Geng *et al. Energy Mater.* **2025**, *5*, 500009
DOI: 10.20517/energymater.2024.46

Energy Materials

Article

Open Access

Check for updates

One-step hydrothermal synthesis of Fe single atom doped 1T-MoS_2 nanosheets for high-performance seawater hydrogen production

Xun Geng[1], Yitong Cao[1], Zhixuan Li[1], Mengyao Li[2], Chaojie Cao[1], Chenxi Yu[1], Xueze Chu[1], Long Hu[2], Yunlong Sun[2], Liang Qiao[3], Xiaojiang Yu[4], Mark B. H. Breese[4], Jang Mee Lee[1], Danyang Wang[2], Dewei Chu[2], Jiabao Yi[1,*]

[1]Global Innovative Centre for Advanced Nanomaterials, School of Engineering, University Drive, The University of Newcastle, Callaghan, NSW 2308, Australia.
[2]School of Material Science and Engineering, The University of New South Wales (UNSW), Sydney 2033, Australia.
[3]School of Physics, University of Electronic Science and Technology of China, Chengdu 610054, Sichuan, China.
[4]Singapore Synchrotron Light Source, National University of Singapore, Singapore 117603, Singapore.

[*]**Correspondence to:** Prof. Jiabao Yi, Global Innovative Centre for Advanced Nanomaterials, School of Engineering, University Drive, The University of Newcastle, University Drive, Callaghan, NSW 2308, Australia. E-mail: Jiabao.yi@newcastle.edu.au

How to cite this article: Geng, X.; Cao, Y.; Li, Z.; Li, M.; Cao, C.; Yu, C.; Chu, X.; Hu, L.; Sun, Y.; Qiao, L.; Yu, X.; Breese, M. B. H.; Lee, J. M.; Wang, D.; Chu, D.; Yi, J. One-step hydrothermal synthesis of Fe single atom doped 1T-MoS_2 nanosheets for high-performance seawater hydrogen production. *Energy Mater.* **2025**, *5*, 500009. https://dx.doi.org/10.20517/energymater.2024.46

Received: 13 May 2024 **First Decision:** 11 Jun 2024 **Revised:** 13 Aug 2024 **Accepted:** 21 Oct 2024 **Published:** 7 Jan 2025

Academic Editor: Sining Yun **Copy Editor:** Ping Zhang **Production Editor:** Ping Zhang

Abstract

In the pursuit of sustainable and clean energy sources, the development of efficient electrocatalysts for hydrogen evolution reaction has gained significant attention. In this work, we synthesized single-atom Fe-doped 1T MoS_2 (sFe-1T/MoS_2) nanosheets using a one-step hydrothermal method, harnessing the synergistic effects of iron-intercalation to enhance hydrogen production through an abundance of active sites. Notably, 10 *at.*% sFe-1T/MoS_2 exhibited excellent hydrogen evolution reaction performance with a low onset potential of 190 mV and a Tafel slope of 55 mV/dec in acidic solution. High performance was also achieved in alkaline solutions. Additionally, these catalysts demonstrated excellent efficiency in seawater splitting. This work not only offers a cost-effective and scalable method for producing high-quality electrocatalysts but also sets a precedent for the application of this technology across various catalytic systems, marking a significant advancement in clean energy research.

Keywords: MoS_2, hydrogen production, single-atoms, seawater splitting

INTRODUCTION

The search for clean energy sources remains the most critical challenge of our time, especially in light of serious consequences induced by greenhouse gas emissions[1]. Hydrogen gas is widely recognized as the cleanest alternative to fossil fuels, as its combustion only produces water. Traditional methods to produce hydrogen are not environmentally friendly due to significant CO_2 emissions. Catalysis is promising to achieve the production of hydrogen with minimal or no greenhouse emissions utilizing processes such as photocatalysis, electrocatalysis, photothermal catalysis, *etc.*[2-5]. Among these, electrocatalysis, a process that produces hydrogen from water using catalysts with a small amount of energy input, has shown great potential for hydrogen clean energy. However, achieving efficient and cost-effective hydrogen production remains challenging, as the expensive Pt catalyst is still the best catalyst due to its outstanding water-splitting efficiency during electrocatalysis (Tafel slope: 30 mV/dec). However, its high cost and scarcity limit its wide applications. Efforts have been made to search for other catalysts as the working electrodes for efficient water splitting, such as graphene, MXene, porous carbons, molybdenum disulfide (MoS_2), *etc.*[6,7]. Among them, MoS_2 has gained considerable attention due to its high conductivity, low synthesis cost and ultra stability during electrocatalysis. MoS_2 features a stable semiconductive phase (2H) and a metastable metallic phase (1T)[8,9]. The 2H phase has limited active sites, making the water splitting less favorable[10]. Specially, the Tafel reaction in water splitting must overcome a high activation energy of 0.98 eV to initiate the Heyrovsky reaction on 2H-MoS_2 basal plane, while 1T phase has a much lower energy barrier of 0.16 eV, followed by a smaller Heyrovsky reaction activation energy (0.62 eV) due to the vibration (S-H edge) at sulfur site in the 1T phase, resulting in a higher hydrogen generation rate on the basal edge of 1T MoS_2[11-14]. However, 1T phase MoS_2 is a metastable phase and achieving long term stable hydrogen production is still challenging. Moreover, its water-splitting performance still has a distance to Pt metals. Therefore, further research is necessary to enhance the performance of 1T-phase MoS_2 by advanced material strategies, such as doping, intercalation, surface modification, *etc.*[3].

Strain engineering has emerged as an effective strategy for stabilizing metastable structures. Our previous work successfully stabilized 1T MoS_2 with hydrazine intercalation. The as-synthesized 1T dominant MoS_2 nanosheets exhibit significantly improved hydrogen evolution reaction (HER) performance (64 mV/dec) with increased active sites, which makes 1T-MoS_2 a bright future for highly efficient water production[15]. Doping, another widely used efficient strategy, introduces multiple lattice strains and defect centers through surface modification. Single-atom doping in electrocatalysis has shown a promising future in terms of catalytic activity, selectivity and stability due to the increased active sites on the catalyst surface[16]. By selecting the appropriate dopants, the electronic properties of the host material can be tailored to optimize catalytic performance. Transition metal featuring a high *d*-orbital status shows a similar effect to Pt on electrocatalysis[17], especially Ni, Cu, V and W, as reported in previous millstones [Supplementary Table 1], showing advanced water splitting efficiency. For example, by doping 5% V, the doped 1T-MoS_2 exhibited a low onset potential of 102 mV and a Tafel slope of 54 mV/dec[7]. The results indicated that doping with transition metals in MoS_2 could effectively modulate the energy level, which decreases the energy barrier for electron transfer and consequently reduces the overpotential. The performance and stability of 1T-MoS_2 can also be improved by intercalating single atoms into its layers. For example, a high concentration of single atoms of copper (98 *at.*%) was successfully intercalated into the layers of 1T MoS_2 by simple stirring. The synthesized Cu-1T MoS_2 optimal sample showed a low onset potential of 104 mV and a small Tafel slope of 52 mV/dec with a high stability and the 1T phase can be maintained up to 800 °C. The enhanced catalytic performance was attributed to improved electrical conductivity, enhanced active sites, and modified electronic structure with weakened H-S bond[18]. Another example includes the work done by Zhao *et al.*, who incorporated FeS_2 clusters with MoS_2, demonstrating a high HER performance with a Tafel slope of 82 $mVdec^{-1}$ and onset potential of 136 mV at a current density of 10 $mAcm^{-2}$[19].

The advancement of electrocatalysts for HER in seawater splitting represents a significant leap toward sustainable hydrogen production. The high efficiency achieved through active ion concentration manipulation underscores the potential for scaling this methodology for industrial applications. Fe is one of the promising transition metals for efficient water splitting due to the S_{2p}-Fe_{3d} interaction[20]. In this work, we develop a single-atom system of Fe-doped 1T MoS_2 (sFe-1T/MoS_2) nanosheets, a material that has recently gained attention for its promising hydrogen electrocatalysis due to the S_{2p}-Fe_{3d} interaction. Notably, the synthesized sFe-1T/MoS_2 nanosheets exhibit a unique structural evolution from single-atom intercalation to site-replacement doping, a phenomenon not extensively documented in previous studies. This structural transformation by doping contributes to a remarkable electrochemical performance, particularly for the 10 *at.*% sFe-1T/MoS_2, which achieves an onset potential of 190 mV and a Tafel slope of 55 mV/dec in acidic solutions. In alkaline solutions, the material displays an extraordinarily low onset potential of 80 mV alongside a slightly higher Tafel slope compared to that in acidic solutions. This dual-performance characteristic in varying pH environments highlights the material's versatility and robustness. The significant enhancement in catalytic activity is attributed to the morphological effects that induced more active sites due to the change in the coordination environment, as confirmed through advanced Near Edge X-ray Absorption Fine Structure (NEXAFS) spectroscopy. Moreover, the synthesized sFe-1T/MoS_2 demonstrates exceptional performance in ocean water splitting, an area of growing interest due to the increasing focus on sustainable and scalable hydrogen production methods. This research provides a novel, facile, and cost-effective strategy for developing highly efficient electrocatalysts, which could revolutionize the field of sustainable energy. Our work not only underscores the potential of sFe-1T/MoS_2 in various electrochemical applications but also paves the way for further exploration of single-atom doped catalysts. The insights gained from this study could inspire the development of next-generation catalytic systems with enhanced performance and durability.

EXPERIMENTAL SECTION

Materials

Fe-doped MoS_2 was synthesized by a hydrothermal reaction. All those chemicals were purchased from Sigma-Aldrich without any further purification. Ammonium heptamolybdate [$(NH_4)_6Mo_7O_{24} \cdot 4H_2O$] was used as the Mo source (*s*Mo) since it matches the microstructure of 1T-MoS_2 because of its fine Mo-centre octahedral structure. $Fe(NO_3)_3 \cdot 9H_2O$ was chosen as the Fe-dopant and the doping concentration varied in a ratio of 2 *at.*%, 5 *at.*%, 10 *at.*% and 20 *at.*%, respectively. First, 10 mmol sulfur powders and 5 mmol *s*Mo were mixed and fully dissolved in 10 ml hydrazine monohydrate ($N_2H_4 \cdot H_2O$) via 20 min ultrasonication. The Fe-dopant was dissolved in 50 ml of deionized (DI) water in another beaker. Then, those two precursors were mixed in 80 mL stainless steel autoclaves for 48 h at 180 °C. The impurities in the product were fully washed using 0.5 M H_2SO_4 and DI water, accompanied by 5000 rpm centrifugation for 15 min. Then, the wet sample was transferred to a vacuum oven for drying for 48 h at room temperature. The pristine 1T-MoS_2 is marked as S0 as the reference compared to the Fe-doped MoS_2 labeled as S2 (2 *at.*%), S5 (5 *at.*%), S10 (10 *at.*%) and S20 (20 *at.*%), respectively. The acidic corrosion to iron-doped MoS_2 was also checked by acidic treatment (2M HCL wash). The prepared samples (800 mg) were put in 50 ml 2M HCL solution with 5 mins stirring. The washed samples were dried in the same way as the sample preparation.

Characterization

The surface morphology was investigated by a JEOL scanning electron microscope (JEOL-SEM) at room temperature. The crystal structure of sFe-1T/MoS_2 was investigated by a JEOL F200 Transmission Electron Microscope (F200-TEM) at 200 kV voltage. X-ray diffraction analysis (XRD) was carried out by a Panalytical Empyrean instrument with λ = 1.54 Å (Cu$K\alpha$) that generates at 40 kV voltage and 40 mA current. The sample was loaded on a circular holder and the angle of measurements is within a 2θ scan range of 5° to 60°. The scan step size is 0.006° with a time-per-step of 97.92s. Raman measurement was

carried out on a Witec alpha-300 spectrometer. A 532 nm laser source was used as the excitation source for 1 h measurement under 0.1% laser power. The textural Brunauer-Emmett-Teller (BET) surface area was determined by the N_2 adsorption-desorption analysis conducted on the Micromeritics ASAP 2420 instrument. The samples were degassed under a constant vacuum at 200 °C before analysis. The degassed samples were analyzed at the liquid nitrogen temperature (-196 °C). The BET method was used to calculate the total specific surface area. Total pore volume was obtained at a relative pressure (P/P0) of 0.99. The micropore characteristics, including the micropore surface area and the micropore volume, were obtained using the t-plot method. The coordination information was also obtained by the low-energy (soft) and high-energy (hard) near-edge X-ray absorption fine structure (NEXAFS) analysis in a total fluorescence yield (TFY) mode at the Synchrotron of Singapore University and the Australia Synchrotron, respectively. X-ray Photoelectron Spectroscopy (XPS) and Ultraviolet Photoelectron Spectroscopy (UPS) were measured by the SPECS Phobis 100 in Chengdu, China. The UPS is performed in He (I) spectrum. All measurements above were taken at room temperature.

Measurements

The electrochemical measurement was carried out using a three-electrode system on CHI 760E electrochemical workstation. The working electrode is the as-deposit samples on glassy-carbon rod electrode (sample loading amount ~ 40 μg·cm^{-2}), Ag/AgCl (3.5 M KCl) and Pt metal was applied as the reference electrode and counter electrode, respectively. 30 mL of 0.5M H_2SO_4 and 1M KOH were used separately as acidic and alkaline electrolytes. Linear sweep voltammetry (LSV) and chronoamperometry were applied with a scan rate of 5.0 mV s^{-1}. The measurements were performed from -0.1 V to -0.8 V (*vs.* Ag/AgCl) in 0.5 M H_2SO_4 and from -0.9 V to -1.6 V (*vs.* Ag/AgCl) in 1.0 M KOH. The LSV performance was also checked in the seawater environment which was picked from the eastern coastline of Newcastle Beach, Australia. All the recorded potentials were then calibrated *vs.* reversible hydrogen electrode (RHE) based on the Nernst equation:

$$\mathrm{E}\ (vs.\ \mathrm{RHE}) = \mathrm{E}\ (vs.\ \mathrm{Ag/AgCl}) + 0.05916 \times \mathrm{pH} + 0.210\ \mathrm{V}$$

The electrochemical impedance spectroscopy (EIS) measurement was carried out at an overpotential of -0.2 V *vs.* RHE over a frequency range from 100 MHz to 10 Hz with an amplitude of 0.005 V. The durability test was applied at the overpotential point of 10 mA cm^{-2} for 43200 seconds (12 h). The electrochemical double-layer capacitance (C_{dl}) was obtained by scanning cyclic voltammetry (CV) within the non-faradaic range, which is equal to the slope of the functional summary between scan rates and average potential (0.2 V *vs.* RHE). Six increasing scan rates (5, 10, 25, 50, 75 and 100 mV/s) were chosen for this measurement. Electrochemically active surface area (EASA) was calculated with the electrochemical double-layer capacitance (C_{dl}) by EASA = C_{dl}/C_s, where C_s is standard specific capacitance (0.02 mF/cm^2) on carbon electrode with a unit surface area.

RESULTS AND DISCUSSION

The XRD patterns of sFe-1T/MoS_2 are presented in Figure 1A. The broad peak at 9.5° indicates the (002) orientation of 1T/MoS_2. Compared to the 2H domain peak at 17.5°, the left-shift peak position indicates the structure change from 2H hexagonal to 1H monolayers, as described in previous works[4,21,22]. The peak position moves slightly to a lower angle when the dopant concentration increases, which indicates the enlarged interlayer space caused by Fe doping. This trend is consistent with our previous work on the Cu single-atom system and suggests the possible formation of single-atom Fe coordination. The impurity peaks in sample S20 indicate the formation of FeS_x clusters (surface aggregation), which is beyond the ideal concentration of iron doping. Raman measurement was also employed to investigate the phase variation of

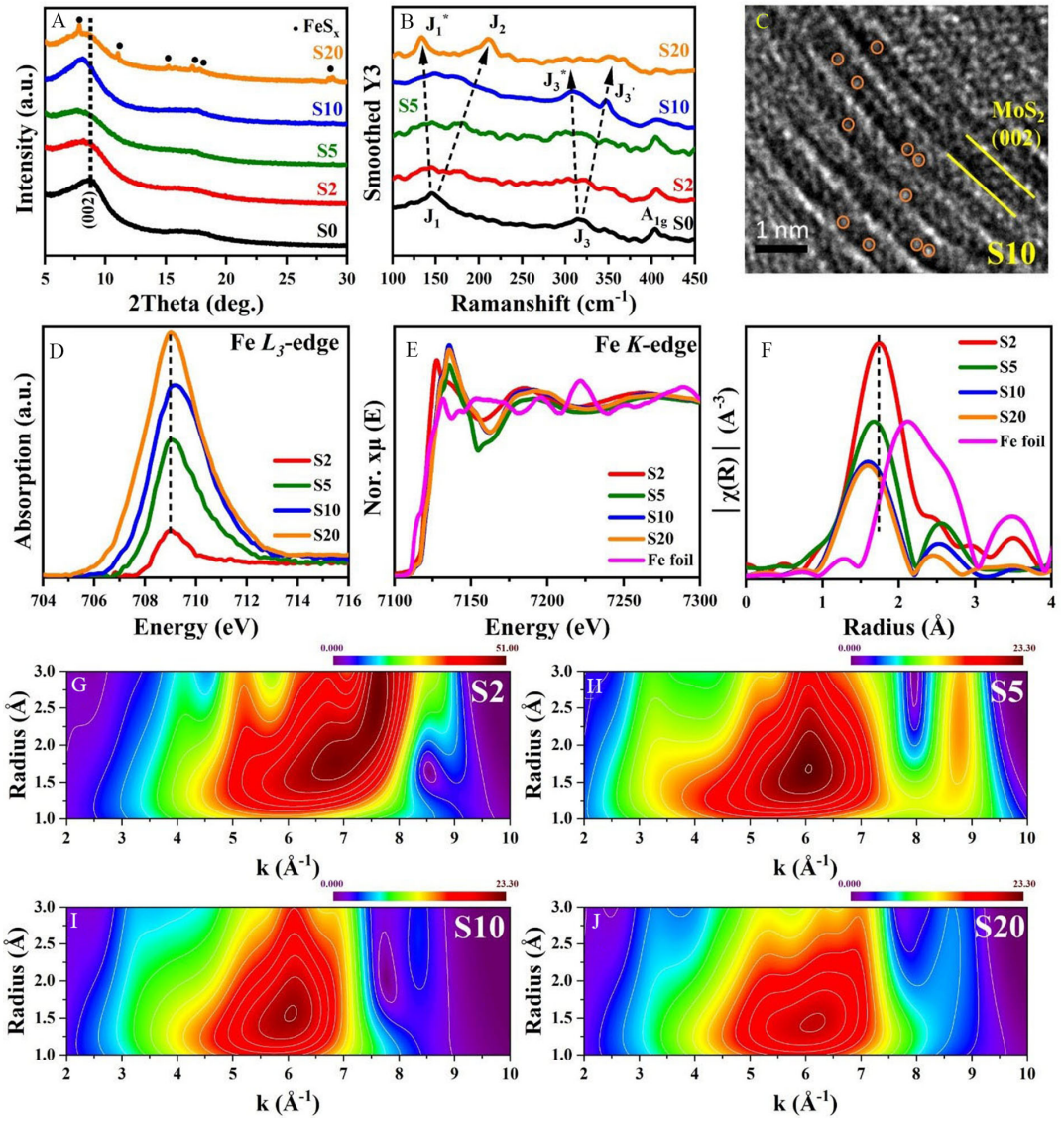

Figure 1. The characterization of sFe-1T/MoS_2. (A) XRD patterns; (B) Raman spectra; (C) High-resolution TEM image of sample S10; (D) XANES curves of Fe L_3-edge; (E) NEXAFS curves of Fe *K*-edge with Fe foil reference; (F) Fourier-transform (FT) k^2-weighted NEXAFS spectra of sFe-1T/MoS_2 with Fe foil reference; Wavelet transform (WT) of k^2-weighted NEXAFS spectra for (G) S2, (H) S5, (I) S10 and (J) S20 based on the mode of Morlet wavelet function ($\kappa = 3$; $\sigma = 0.5$) for the first coordination shells, where $1 \le (R+\alpha) \le 3$ Å and $2 \le k \le 10$ Å^{-1}. XRD: X-ray diffraction analysis; TEM: Transmission electron microscope; NEXAFS: Near edge X-ray absorption fine structure; XANES: X-ray absorption near edge structure.

sFe-1T/MoS_2. As displayed in Figure 1B, 1T- dominant bond vibration is confirmed by intense peaks at the Raman shift of 147 and 324 cm^{-1} for 1T-phase J_1 (out of plane) and J_3 (in-plane) Mo-S phonon modes, respectively[23]. As the dopant concentration increases, a leftward shift of the J_1 peak ($J_1 \rightarrow J_1^*$) with a broadened peak area (S0 → S10) indicates changes in anisotropic symmetry due to Fe doping, while a J_2 mode is also presented in sample S20. Generally, the J_2 vibrational mode is related to in-plane Mo-S displacements (defects). This indicates weak zigzag (S-Mo-S) displacements at low doping concentrations supported by single-atom intercalation[24]. While the strong site replacement effect is observed at high doping concentrations (S20) instead of layer intercalation. Additionally, peak splitting is also observed for the in-plane J_3 vibrational mode ($J_3 \rightarrow J_3^*$ and $J_3 \rightarrow J_3'$, respectively) and the J_3 peak suddenly disappears in

sample S20. The pronounced peak splitting highlights the twofold symmetric variation between single-atom doping and site replacement doping and also indicates doping-induced phase variation from 1T to 2H[25]. Furthermore, the peak at 407 cm^{-1} corresponds to the out-of-plane S-Mo-S opposite moving (A_{1g}) of MoS_2. The peak intensity of A_{1g} mode decreases without a noticeable peak position shift, suggesting a weakening of out-of-plane S-Mo-S vibrations due to a formation of S-Fe-S bulks (phase aggregation), agreeing with the SEM results described above. The absence of the E_{1g} mode is primarily attributed to low laser density as a laser-induced 1T to 2H phase transition can be triggered under high laser density conditions[26]. The deep lattice pattern is further demonstrated by transmission electron microscopy (TEM) from sample S0 to sample S10. The high-resolution TEM image of sample S10 is displayed in Figure 1C and that of others is demonstrated in Supplementary Figure 1. The apparent wrinkles indicate the fine sheet structure of sFe-1T/MoS_2 at low doping concentrations. Some Fe atoms are found between interlayers of MoS_2 without prominent Fe clusters, suggesting the formation of single atoms. In addition, there is a plane expansion (002) in doped MoS_2 1T-dominance, from 0.83 nm to 0.98 nm, when the doping concentration increases from 0 to 10 *at.*%. Those observations prove the Fe single-atoms intercalation between MoS_2 layers, consistent with our previous works on Cu intercalated 1T/MoS_2[18].

To understand the electron environment of iron intercalation, the L_3-edge orbital status of iron is explained by low-energy (soft) NEXAFS measurement to determine the dynamic process of p-d dipole excitation, as demonstrated in Figure 1D. The 2p → 3d electron transfer occurs between 708 eV and 710 eV without obvious t_{2g}-e_g orbital splitting in all samples. Additionally, only an L_3 p-d electron transfer peak is observed at 709 eV, indicating the absence of strong crystal field splitting effect. This behavior is mainly attributed to the low spin state (unoccupied e_g dominant) of Fe^{2+}[27]. A slightly right shift of peak position (S2 → S10) indicates a lower coordination environment and higher oxidization state since a lower valence band position can be predicted[28]. However, there is no shift for sample S20, which is associated with the structural aggregation mentioned above. The peak intensity increases and the peak width also broadens symmetrically aligned with the rise in Fe concentrations (S2 → S10). Generally, the higher peak intensity indicates a higher unoccupied density state (more empty orbitals) and lower covalency caused by higher dopant concentration[29]. In contrast, the enlarged peak width indicates the expanded unoccupied orbitals and enhanced orbital contributions caused by multi-coordination[30]. It is observed that there is no obvious post-edge shift from samples S10 to S20, while a pre-edge shift is noticeable. This indicates the new subband formed aligning with the transition from a low spin multiplet (unoccupied e_g dominant) to high spin multiplet (t_{2g}/e_g equal contribution) transition when the Fe concentration keeps increasing (new phase generated)[31]. Fe *K*-edge (1s → 4p dipole electron transition) is further checked by high energy (hard) NEXAFS and the normalized adsorption edge is displayed in Figure 1E. Generally, the shift of edge position is associated with the change of oxidization state, such as the transition from ferrous to ferric. All samples show a higher edge position than the reference curve of Fe foil, which confirms the similar oxidization state (Fe^{2+}) of iron in sFe-1T/MoS_2. A pre-edge peak at 7,113 eV for sample S20 is observed compared to a flat appearance in samples with lower doping concentrations. The pre-edge feature originates from a quadrupole (1s to 3d) transition, indicating a 3d→4p geometric coordination hybridization from octahedral to tetrahedral (T_d) symmetry, accordingly[32]. It also has a rising edge level (7,115 ~ 7,120 eV) from S2 to S20, while this edge lifting between 7,115 eV and 7,120 eV, in our case, is mainly affected by the pre-edge feature aligning with the increased dopant concentration since there is no noticeable edge position shift to Fe-doped samples. The feature peak at 7,120 eV in sample S20 indicates the bulk formation of FeS_2. This is confirmed by SEM images [Supplementary Figure 2]. The nanoflower appearance (S0 → S10) indicates fine nanosheet structure of MoS_2, shrinking in dry conditions, while a bulk-like morphology is observed in sample S20. This proves a sheet to bulk transition with increased doping concentration, which is widely observed in other doping systems. The intensity of the adsorption peak at 7,127 eV decreases, accompanied by an elevated peak intensity at 7,135 eV when dopant concentration grows to 5 *at.*%, which corresponds to

the standard FeS to FeS_2 transition[33]. A slightly decreased peak intensity from samples S5 to S20 is mainly caused by orbital distortion, corresponding to the pre-edge changes. The distance of the first atom shell is obtained by Fourier k^2-weighted transform (k^2-FT), as shown in Figure 1F. Compared to the Fe-Fe scattering path in Fe foil (2.2 Å), the absence of Fe–Fe interaction indicates the single-atom configuration for sFe-1T/MoS_2. The peak at approximately 1.7 Å is mainly attributed to the first shell Fe-S scattering path coordinated at the S site between the basal planes[34]. In addition, there is a slight peak shifting to a shorter scattering path to 1.5 Å with the increased Fe concentration where a decreased peak intensity of the Fe-S distribution is aligned, which is associated with a reduced Fe-S coordination number and the oscillation from octahedral to tetrahedral coordination environment[35]. The reliability of Fourier transform (FT) is further confirmed by the forward-backward FT ($k \rightarrow R \rightarrow q$). The good matching between k-space and q-space curves confirms the reliable results of FT, as displayed in Supplementary Figure 3. Wavelet-transformed analysis of *R*-space curves by the Morlet function is also conducted to differentiate the spatial interactions of the Fe atoms. As displayed in Figure 1G-J, the energy maximum (*k*-space) for all samples is located in the range of 5-7 $Å^{-1}$, falling in the standard Fe-S bonding range[36,37]. This again supports that the Fe species are individually dispersed as Fe-S single-atom coordination. This status of Fe is also proved by XPS surface characterization. The positions of Fe_{2p}, Mo_{3d} and S_{2p} peaks are labeled in the XPS survey curves shown in Supplementary Figure 4. The C_{1s} and O_{1s} peaks arise from the carbon tape background due to sample loading. No pronounced Fe peaks are examined except in sample S20, which indicates the embedded Fe-single atoms between interlayers of MoS_2 at low doping concentrations.

The catalysis performance for HER was investigated by three-electrode LSV measurement. As displayed in Figure 2A, the HER performance of the sFe-1T/MoS_2 (S2, S5 and S10) is gradually improved by the increased dopant concentration compared to pristine 1T/MoS_2 nanosheets in an acidic solution. Iron-doped samples exhibit better HER performances with decreased overpotentials. In particular, sample S10 shows the best performance with an onset potential of 190 mV *vs.* RHE and an overpotential of 215 mV *vs.* RHE [Supplementary Table 2]. Tafel slope is generally used to identify the HER mechanism consisting of the Volmer-Tafel and Volmer-Heyrovsky process and determine the rate-controlling step for a certain catalyst. It has been reported that 1T/MoS_2 follows standard Volmer-Heyrovsky process[38]. As displayed in Figure 2B, the low Tafel slope of sample S0 (70 mV/dec) indicates high catalytic performance of 1T/MoS_2 corresponding to our previous report on ultra-stable 1T-phase MoS_2 nanosheets[15]. Volmer process ($H_3O^+ + e^- = H_{ads}$) is a fast process with a low energy barrier, but if it is under rate-limiting control, the Tafel slope would be much higher[12]. It has been reported that if a fast discharge reaction (Volmer) is followed by a rate-limiting Tafel combination reaction, Heyrovsky ($H_{ads} + H_3O^+ + e^- = H_2$) dominates, leading to a low Tafel slope; While if a fast Volmer discharge reaction is followed by a slow Heyrovsky electrochemical desorption reaction, Tafel process ($H_{ads} + H_{ads} = H_2$) dominates, leading to a high Tafel slope[39]. After doping with Fe, the Tafel slope of MoS_2 decreases from 70 to 55 mV/dec in sample S10, suggesting the increased coverage of H and adsorption-desorption kinetics. In electrocatalysis, inherently excellent conductivity tends to afford rapid electron transport and extend electrons to more active sites, thus resulting in increased utilization efficiency of active sites[40]. The decreased Tafel slope also shows a far lower electrochemical desorption process on sFe-1T/MoS_2 surface indicating higher EASA. As EASA can be an indicator of the number of active sites, it confirms that Fe dopant further induces rich active sites on 1T-MoS_2. Therefore, the EASA is calculated from the non-Faradaic region of the CV curves with the increased scan rates [Supplementary Figure 5]. The summarized fitting plots have been displayed in Figure 2C for C_{dl} calculation. The EASA value is dramatically enhanced, from 4,165 cm^2 to 5,853 cm^2, by the increased dopant concentration from samples S0 to S10 caused by the increased active sites of basal planes. The EASA value drops significantly for sample S20, which indicates a morphology change under a high doping level. To further evaluate this property, BET surface area was measured as shown in Supplementary Figure 6 in the supporting information. The surface area of sFe-1T/MoS_2 rises from 8.6 m^2/g to 17.38 m^2/g from sample S2

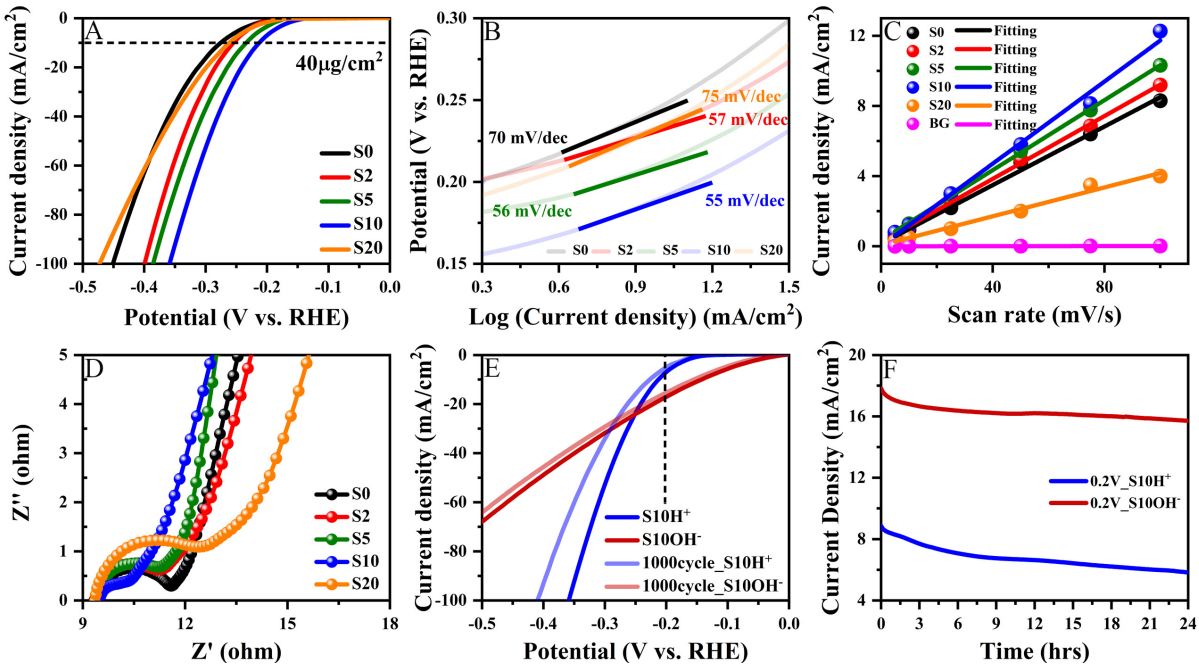

Figure 2. Electrochemical measurements for all Fe-1T/MoS_2 samples. (A) LSV measurements in 0.5 M H_2SO_4 solution; (B) Tafel slopes derived from LSV curves; (C) Fitting plots of C_{dl} from CV measurements for the EASA calculation; (D) The EIS in 0.5 M H_2SO_4 solution; (E) The stability measurements for the acidic and alkaline solution for sample S10; (F) 24 h stability measurement at a constant RHE potential of - 0.2 V (equal to 10 mA/cm^2 current density in acidic (0.5 M H_2SO_4) and alkaline (1M KOH) solutions, respectively. LSV: Linear sweep voltammetry; RHE: Reversible hydrogen electrod; CV: Cyclic voltammetry; EASA: Electrochemically active surface area; EIS: Electrochemical impedance spectra.

to sample S10, consistent with the trend in CV measurement, thus supporting the presence of the more active sites in the S10 sample. In addition, BET surface area decreases to 6.35 m^2/g with rising doping concentration (S20), corroborating surface aggregation under high doping concentrations, as demonstrated in XRD results[41]. Electrochemical impedance spectra (EIS) are demonstrated in Figure 2D. The decreased semi-circle diameter, from samples S0 to S10, indicates the reduced resistance with enhanced iron concentration[42]. This is primarily caused by the high concentration of iron single atoms in MoS_2 layers, leading to excellent LSV results and catalytical performance. The enlarged contact resistance of sample S20 is mainly caused by surface-aggregated FeS_x bulks. For the non-doped sample, there is minor Tafel slop variation and a change of onset potential. Figure 2E shows the stability measurement in acidic and alkaline environments. Since the iron site is sensitive to catalytical environment, the long-term stability of sample S10 is further checked in both acidic (0.5 M H_2SO_4) and alkaline solution (1M KOH) referring to the non-doped sample (S0) in Supplementary Figure 7 of supporting information. In alkaline solution, after 1,000 cycles, there is not much change in terms of onset potential and Tafel slope, suggesting that the active sites on MoS_2 basal are mainly attributed to the iron doping because of lower chemical corrosion in alkaline environment. However, for stability in an acidic solution, the LSV curves change significantly after 1,000 cycles. This may be due to the acidic corrosion of single Fe atoms. To understand the mechanism, the Fe-1T/MoS_2 is treated with 1M HCL solution and we observed the structural changes. After acidic treatment, a broader peak is observed for all samples [Supplementary Figure 8A-E]. When the reaction between iron active sites and acidic solution happens, the iron between MoS_2 layers will be extracted, causing layer collapse and d-spacing narrowing [Supplementary Figure 8F]. This high acidic sensitivity should be associated with single-atom nature of Fe in MoS_2 layers. Figure 2F shows the time-dependent measurement of current density at an overpotential of -0.2 V. In acidic solution, the current density decays continuously

until stable after 6 h. In alkaline solution, there is an apparent decline in current density at the beginning and then the current density gradually becomes stable. The overall stability of the sample in alkaline solution is better than that in acidic solution, which may be due to the corrosion in the acidic environment. Stability tests were carried out at the RHE potential of -0.3 V and -0.5 V, respectively, as shown in Supplementary Figure 9 in the supporting information. When the potential is at -0.3 V, the sample showed an excellent stability, while when the potential reached -0.5 V, the current density continuously decreased in the first five hours. The sample current density became stable.

To investigate the mechanism of the enhanced HER, the valence band structure was examined by UPS (HeI) measurement and the overall spectra are displayed in Supplementary Figure 10. There is no obvious drift in ionization energy for all 1T-MoS_2 samples, indicating that the enhancement of HER is related to more active sites induced by coordination environment change instead of doping-related work function variation[40]. The zoom-in spectra of UPS are demonstrated in Figure 3A to check the variation in 2p orbitals. In the Fe single atom system, the peak of 2p orbitals shifts slightly to lower binding energy from 6.5 eV to 6.3 eV from samples S0 to S2. This is mainly caused by the newly formed van der Waals force between Fe and S. There is no peak shift from S2 to S10 with slightly decreased peak intensity. This indicates a reproductive single-atom state for our samples. The decreased peak intensity is mainly caused by layer expansion-induced orbital variation that resulted from higher intercalation concentration. The peak of S20 shows dramatic shifting on both peak position and intensity, which results from the transition from Fe-S Van der Waals force to covalent Fe-S bond which is promoted by the p-d overlapping in atom replacement doping system and surface aggregation as mentioned before[43]. This process is also demonstrated by d-orbital variation in Figure 3B. The peak at 1.18 eV is contributed by d orbital of MoS_2. The peak intensity decreases from S0 to S10 and increases significantly for sample S20, confirming the observation in Figure 3A that the enhanced orbital hybridization is mainly caused by new-formed FeS_x bulks[44]. The peak variation in UPS also indicates the change of coordination environment. The coordination environment of Fe is fitted by NEXAFS curves and summarized in Figure 3C. The fitting curve well matches both real and imaging parts of the fitting curve [Supplementary Figure 11] and low Debye-Waller factors [Supplementary Table 3], indicating reliable fitting results. The coordination number decreases from 6.5 to 5 from S2 to S20. In a typical FeS_2 crystal, Fe atoms are coordinated by six ligands, forming a stable and sulfur-rich coordination environment. A higher coordination number in low iron concentration sample (S2) suggests the co-existence of N-Fe-S interlayer chains. These chains represent a significant electron supply from the standard FeS_2 configuration. The formation of these interlayer chains not only increases the coordination number but also introduces new types of Fe sites that are likely more catalytically active due to their altered electronic structure[45,46]. The observed reduction in coordination numbers in sample S10 signifies a diminish of the electronegative environment around the Fe atoms, which effectively increases the local electron density at Fe sites, which is crucial to engage in electron transfer reactions and push the Fe sites to be more reactive in an acidic environment. As mentioned above, the HER process of MoS_2 relies on one primary discharge step and at least one kind of desorption step. The activation effect on hydroxonium ion (H_3O^+) goes through synergistic interaction along Fe-S-H chain, as roughly represented in Figure 3D. The catalysis kinetics depend on a delicate balance between the dissociation rate of H_3O^+ on $Fe^{\delta+}$ site in acidic solution, the recombination rate of H_{ads} on $S^{\delta-}$ site and the desorption rate of H_2O, which helps to accommodate the adsorption of the next H_3O^+ molecules. During the discharge step, H_3O^+ diffuses to the catalyst surface and then H_3O^+ picks up electrons and generates hydrogen adsorbed on the catalyst surface. In the current system, due to the synergistic interaction between Fe and H, the concentration of available H_3O^+ is increased, hence facilitating the discharge process[47]. While in an alkaline solution, OH^- directly pushes free H_{ads} to the S site, jumping over the process of synergistic interaction along the Fe-S-H chain. In this case, the electron-rich center moves from Fe to S, which can explain the difference between acidic and alkaline solutions.

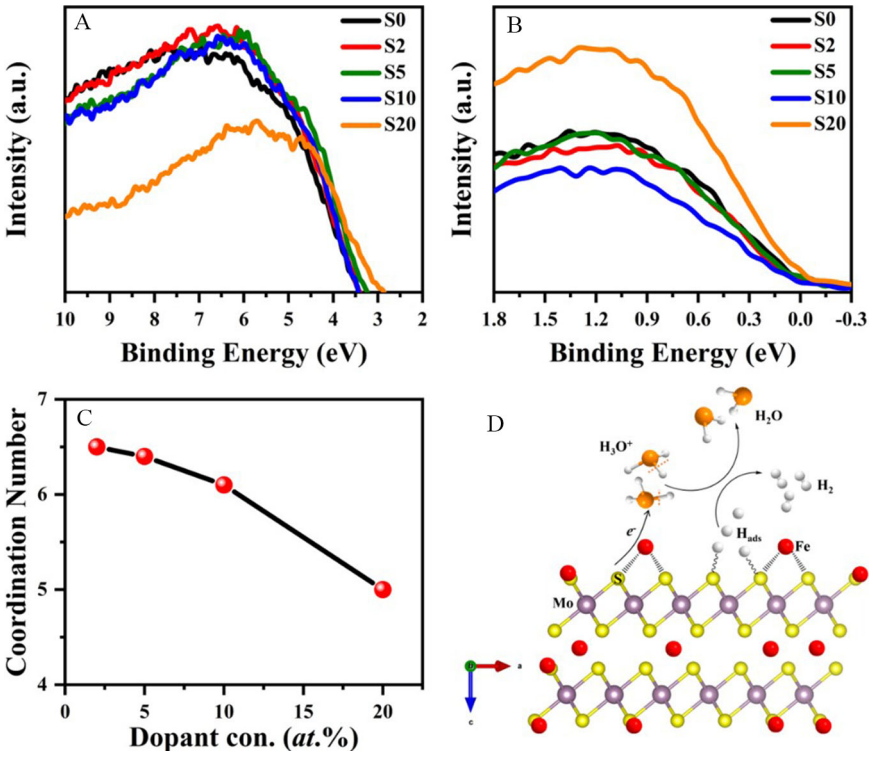

Figure 3. (A)-(B) UPS (HeI) spectra of s-Fe-1T/MoS_2; (C) Coordination number changes with increased Fe concentration; (D) Schematic diagram of catalysis process of sFe-1T/MoS_2. UPS: Ultraviolet photoelectron spectroscopy.

To further validate our findings, we applied two additional RHE potentials of -0.3 V and -0.5 V during the stability test. The X-ray absorption spectroscopy (XAS) results for sample S10 after catalysis are presented in Supplementary Figure 12 in the supporting information. As shown in Supplementary Figure 12A, there are no significant changes in the pre-edge peak before and after catalysis at an RHE potential of -0.3 V, indicating minimal variation in the coordination environment after catalysis. However, an increase in the quadrupole pre-edge peak intensity was observed with prolonged catalysis at -0.5V, suggesting a shift towards a higher electronegativity and a more asymmetric coordination environment. The edge position also shifts to a higher energy range, from 7,120 eV to 7,125 eV, reflecting an increase in the Fe oxidation state and the formation of a higher electronegativity center, consistent with the pre-edge changes. Additionally, a new merged white peak at 7,130 eV emerges post-catalysis compared to the split peak observed before catalysis, indicating a newly formed dominant p orbital contribution. This p orbital contribution diminishes when the catalysis was performed at high potential, which suggests the S-site peeling off at high-voltage catalysis. The R-space curves, displayed in Supplementary Figure 12B, further support these observations. A reduction in atomic distance from approximately 1.8 Å to 1.4 Å is observed, along with a decrease in peak intensity. It suggests a reduced coordination number of the Fe site with an indicative transition from FeS_x to FeO_x.

More active sites induced by iron single atoms also promote significant enhancement in real industrial applications, such as ocean water splitting. In normal ocean water, lower OH^-/H^+ concentration (neutral pH) leads to a low catalytical efficiency. Thus, to evaluate the efficiency of ocean water splitting, 10% v/v and 30% v/v 0.5M H_2SO_4 and 1M KOH solutions were added to the ocean water, respectively. The performance in pure acidic and alkaline solutions is remarked as S-H100 and S-OH100, respectively, as the standard reference. The LSV curves of ocean water splitting are demonstrated in Figure 4A and the overpotential at

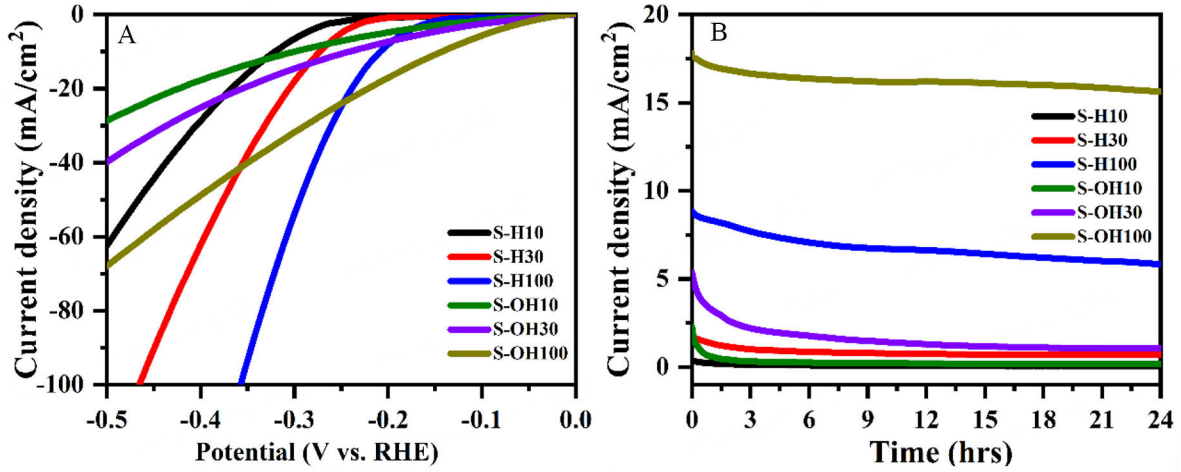

Figure 4. (A) Seawater HER performance with different volume ratios (v/v) of 0.5M H_2SO_4 and 1M KOH. The concentration is 10% v/v (S-H10/S-OH10), 30% v/v (S-H30/S-OH30) and 100% v/v (pure solution, S-H100/S-OH100), respectively; (B) The long-term stability in such a solution is tested at a constant RHE potential of -0.2 V within 24 h. HER: Hydrogen evolution reaction; RHE: Reversible hydrogen electrode.

10 mAcm^{-2} has been summarized in Supplementary Table 4 supported by previous milestones in MoS_2-based seawater splitting. Tafel slope keeps increasing when pH is close to a neutral level, which is mainly caused by reduced active catalytic ions in the environment. This also indicates the reliability of electrocatalytical performance for sFe-1T/MoS_2. The long-term stability was also checked, as displayed in Figure 4B. Catalysts in acidic solution show a similar trend with different H^+ concentrations, indicating stable performance of acidic ocean splitting. A serious decay is observed in the initial stage (within 3 h) for alkaline-modified ocean water compared to pure 1M KOH solution. This is mainly caused by the newly formed Ca/Mg-based carbonates in the ocean water, which block the active surface of MoS_2 and significantly reduce the performance of water splitting. This also explains why this phenomenon is not obvious in acidic solution since it is corroded immediately in H^+ environment. The overpotential at 10 mA/cm^2 reaches 242 mV for the S-OH30 sample, which is relatively lower compared to previous MoS_2 catalysis. In addition, chloride ions in seawater will also significantly affect the HER by competing with hydrogen ions for adsorption sites on the electrode surface, thereby reducing the efficiency of hydrogen production. This explains the significant decrease in current density observed in seawater compared to pure acidic and alkaline solutions. In addition, the chloride ion in seawater also significantly influences HER performance by competing with hydrogen ions on adsorption sites of electrodes, reducing the efficiency of hydrogen production consequently. This competition results in a notable decrease in current density observed in seawater environment compared to pure acidic and alkaline solutions. Furthermore, Cl^- can induce electrode corrosion. Although the corrosive effect in alkaline solutions is less effective than in neutral or acidic environments, chloride-induced sample peeling off is the primary concern since Cl ions can penetrate protective oxide layers on the electrode surface, leading to localized corrosion and subsequent the degradation of the electrode's structural integrity.

CONCLUSION

In this work, single-atom iron-modified 1T/MoS_2 was synthesized using a scalable hydrothermal method. The synthesized samples showed structure transformation from single-atom intercalation to site replacement doping with increasing doping concentrations. Our results demonstrate that doping concentration can significantly influence the HER performance of the doped 1T-phase MoS_2. The 10% *at.* sFe/1T/MoS_2 exhibited superior electrochemical activity toward HER with an onset potential of 190 mV and

a Tafel slope of 55 mV/dec in acidic solution. Additionally, it shows an exceptionally low onset potential of 80 mV, albeit with a slightly higher Tafel slope in alkaline solution, indicating distinct HER mechanisms. The substantial enhancement is attributed to the morphological effect-induced rich active sites due to the change of coordination environment. Additionally, the synthesized product also exhibited high efficiency in ocean water splitting with an overpotential of 242 mV at 10mA/cm^2 in a 30%v/v mixed KOH/seawater environment. This high efficiency of seawater splitting is primarily attributed to the active ions. Our present work provides a facile and cost-effective strategy for designing efficient electrocatalysts for HER, promising broad applicability of this methodology to other catalytic systems. However, overcoming electrode corrosion and achieving high-power output ocean catalysis remain significant challenges requiring further investigation.

DECLARATIONS

Authors' contributions

Mainly supervised this project: Yi, J.
Carried out this project: Geng, X.
Contributed to sample characterization: Cao, Y.
Performed TEM measurements: Li, Z.
Assisted with catalysis measurement: Li, M.; Chu, D.
Contributed to the materials characterization and revised the manuscript: Cao, C.; Yu, C.; Chu, X.; Hu, L.; Sun, Y.; Wang, D.; Qiao, L.
Conducted the NEXAS measurements: Yu, X.; Breese, M. B. H.
Conducted the EXAFS measurements: Lee, J. M.

Availability of data and materials

The data that support the findings of this study are available from the corresponding author upon reasonable request.

Financial support and sponsorship

This work was supported by the Australian Research Council (DP220103045). The authors would like to acknowledge the Singapore Synchrotron Light Source for providing the facility necessary for conducting the research. The Laboratory is a National Research Infrastructure under the National Research Foundation, Singapore. Any opinions, findings, conclusions or recommendations expressed in this material are those of the author(s) and do not reflect the views of the National Research Foundation, Singapore.

Conflicts of interest

All authors declared that there are no conflicts of interest.

Ethical approval and consent to participate

Not applicable.

Consent for publication

Not applicable.

REFERENCES

1. Liu, Z.; Deng, Z.; Davis, S. J.; Giron, C.; Ciais, P. Monitoring global carbon emissions in 2021. *Nat. Rev. Earth. Environ.* **2022**, *3*, 217-9. DOI PubMed PMC
2. Fan, P.; He, Y.; Pan, J.; et al. Recent advances in photothermal effects for hydrogen evolution. *Chinese. Chem. Lett.* **2024**, *35*, 108513. DOI
3. Chu, X.; Sathish, C. I.; Yang, J. H.; et al. Strategies for Improving the photocatalytic hydrogen evolution reaction of carbon nitride-based catalysts. *Small* **2023**, *19*, e2302875. DOI
4. Yadav, A. A.; Hunge, Y. M.; Dhodamani, A. G.; Kang, S. W. Hydrothermally synthesized Ag@MoS_2 composite for enhanced photocatalytic hydrogen production. *Catalysts* **2023**, *13*, 716. DOI
5. Yadav, A.; Hunge, Y.; Kang, S. Porous nanoplate-like tungsten trioxide/reduced graphene oxide catalyst for sonocatalytic degradation and photocatalytic hydrogen production. *Surf. Inter.* **2021**, *24*, 101075. DOI
6. Cui, C.; Xie, J.; Lin, D.; et al. Recent progress in carbon-based materials as catalysts for electrochemical and photocatalytic water splitting. In: Paul R, Etacheri V, Wang Y, Lin CT , Editors. Carbon based nanomaterials for advanced thermal and electrochemical energy storage and conversion. Elsevier; 2019.p.173-200. DOI
7. Li, M.; Cai, B.; Tian, R.; et al. Vanadium doped 1T MoS_2 nanosheets for highly efficient electrocatalytic hydrogen evolution in both acidic and alkaline solutions. *Chem. Eng. J.* **2021**, *409*, 128158. DOI
8. Wang, D.; Zhang, X.; Bao, S.; Zhang, Z.; Fei, H.; Wu, Z. Phase engineering of a multiphasic 1T/2H MoS_2 catalyst for highly efficient hydrogen evolution. *J. Mater. Chem. A.* **2017**, *5*, 2681-8. DOI
9. Li, M.; Kuo, Y.; Chu, X.; Chu, D.; Yi, J. MoS_2 nanoflower incorporated with Au/Pt nanoparticles for highly efficient hydrogen evolution reaction. *Emergent. Mater.* **2021**, *4*, 579-87. DOI
10. Jaramillo, T. F.; Jørgensen, K. P.; Bonde, J.; Nielsen, J. H.; Horch, S.; Chorkendorff, I. Identification of active edge sites for electrochemical H_2 evolution from MoS_2 nanocatalysts. *Science* **2007**, *317*, 100-2. DOI
11. Lin, Y. C.; Dumcenco, D. O.; Huang, Y. S.; Suenaga, K. Atomic mechanism of the semiconducting-to-metallic phase transition in single-layered MoS_2. *Nat. Nanotechnol.* **2014**, *9*, 391-6. DOI PubMed
12. Tang, Q.; Jiang, D. Mechanism of hydrogen evolution reaction on 1T-MoS_2 from first principles. *ACS. Catal.* **2016**, *6*, 4953-61. DOI
13. Li, W.; Liu, G.; Li, J.; et al. Hydrogen evolution reaction mechanism on 2H-MoS_2 electrocatalyst. *Appl. Surf. Sci.* **2019**, *498*, 143869. DOI
14. Tang, J.; Huang, J.; Ding, D.; Zhang, S.; Deng, X. Research progress of 1T-MoS_2 in electrocatalytic hydrogen evolution. *Int. J. Hydrogen. Energ.* **2022**, *47*, 39771-95. DOI
15. Li, M.; Zhou, Z.; Hu, L.; et al. Hydrazine hydrate intercalated 1T-dominant MoS_2 with superior ambient stability for highly efficient electrocatalytic applications. *ACS. Appl. Mater. Inter.* **2022**, *14*, 16338-47. DOI
16. Lei, Z.; Sathish, C.; Liu, Y.; et al. Single metal atoms catalysts-promising candidates for next generation energy storage and conversion devices. *EcoMat* **2022**, *4*, e12186. DOI
17. Levy, R. B.; Boudart, M. Platinum-like behavior of tungsten carbide in surface catalysis. *Science* **1973**, *181*, 547-9. DOI
18. Li, M.; Selvarajan, P.; Wang, S.; et al. Thermostable 1T-MoS_2 nanosheets achieved by spontaneous intercalation of Cu single atoms at room temperature and their enhanced HER performance. *Small. Struct.* **2023**, *4*, 2300010. DOI
19. Zhao, X.; Ma, X.; Lu, Q.; et al. FeS_2-doped MoS_2 nanoflower with the dominant 1T-MoS_2 phase as an excellent electrocatalyst for high-performance hydrogen evolution. *Electrochim. Acta.* **2017**, *249*, 72-8. DOI
20. Huang, W.; Zhou, D.; Qi, G.; Liu, X. Fe-doped MoS_2nanosheets array for high-current-density seawater electrolysis. *Nanotechnology* **2021**, *32*, 415403. DOI
21. Acerce, M.; Voiry, D.; Chhowalla, M. Metallic 1T phase MoS_2 nanosheets as supercapacitor electrode materials. *Nat. Nanotechnol.* **2015**, *10*, 313-8. DOI PubMed
22. Liu, L.; Wu, J.; Wu, L.; et al. Phase-selective synthesis of 1T' MoS_2 monolayers and heterophase bilayers. *Nat. Mater.* **2018**, *17*, 1108-14. DOI
23. Geng, X.; Sun, W.; Wu, W.; et al. Pure and stable metallic phase molybdenum disulfide nanosheets for hydrogen evolution reaction. *Nat. Commun.* **2016**, *7*, 10672. DOI PubMed PMC
24. Nayak, A. P.; Pandey, T.; Voiry, D.; et al. Pressure-dependent optical and vibrational properties of monolayer molybdenum disulfide. *Nano. Lett.* **2015**, *15*, 346-53. DOI
25. Park, M. J.; Yi, S. G.; Kim, J. H.; Yoo, K. H. Metal-insulator crossover in multilayered MoS_2. *Nanoscale* **2015**, *7*, 15127-33. DOI PubMed
26. Nam, G. H.; He, Q.; Wang, X.; et al. In-plane anisotropic properties of 1T'-MoS_2 layers. *Adv. Mater.* **2019**, *31*, e1807764. DOI
27. Groot, F. D. Multiplet effects in X-ray spectroscopy. *Coordin. Chem. Rev.* **2005**, *249*, 31-63. DOI
28. Mohamed, A. Y.; Park, W. G.; Cho, D. Y. Chemical structure and magnetism of FeO_x/Fe_2O_3 interface studied by X-ray absorption spectroscopy. *Magnetochemistry* **2020**, *6*, 33. DOI
29. Hocking, R. K.; DeBeer, G. S.; Raymond, K. N.; Hodgson, K. O.; Hedman, B.; Solomon, E. I. Fe L-edge X-ray absorption spectroscopy determination of differential orbital covalency of siderophore model compounds: electronic structure contributions to high stability constants. *J. Am. Chem. Soc.* **2010**, *132*, 4006-15. DOI PubMed PMC
30. Hocking, R. K.; Wasinger, E. C.; Yan, Y. L.; et al. Fe L-edge X-ray absorption spectroscopy of low-spin heme relative to non-heme Fe complexes: delocalization of Fe d-electrons into the porphyrin ligand. *J. Am. Chem. Soc.* **2007**, *129*, 113-25. DOI

31. Baker, M. L.; Mara, M. W.; Yan, J. J.; Hodgson, K. O.; Hedman, B.; Solomon, E. I. K- and L-edge X-ray absorption spectroscopy (XAS) and resonant inelastic X-ray scattering (RIXS) determination of Differential orbital covalency (DOC) of transition metal sites. *Coord. Chem. Rev.* **2017**, *345*, 182-208. DOI PubMed PMC
32. Westre, T. E.; Kennepohl, P.; Dewitt, J. G.; Hedman, B.; Hodgson, K. O.; Solomon, E. I. A multiplet analysis of Fe K-edge 1s → 3d pre-edge features of iron complexes. *J. Am. Chem. Soc.* **1997**, *119*, 6297-314. DOI
33. Kitajou, A.; Yamaguchi, J.; Hara, S.; Okada, S. Discharge/charge reaction mechanism of a pyrite-type FeS_2 cathode for sodium secondary batteries. *J. Power. Sources.* **2014**, *247*, 391-5. DOI
34. Mo, J.; Wu, S.; Lau, T.; et al. Transition metal atom-doped monolayer MoS_2 in a proton-exchange membrane electrolyzer. *Mater. Today. Adv.* **2020**, *6*, 100020. DOI
35. Pattengale, B.; Huang, Y.; Yan, X.; et al. Dynamic evolution and reversibility of single-atom Ni(II) active site in 1T-MoS_2 electrocatalysts for hydrogen evolution. *Nat. Commun.* **2020**, *11*, 4114. DOI PubMed PMC
36. Zheng, J.; Wu, S.; Lu, L.; et al. Structural insight into [Fe-S_2-Mo] motif in electrochemical reduction of N_2 over Fe_1-supported molecular MoS_2. *Chem. Sci.* **2020**, *12*, 688-95. DOI
37. Ye, J.; Zang, Y.; Wang, Q.; et al. Nitrogen doped FeS_2 nanoparticles for efficient and stable hydrogen evolution reaction. *J. Energy. Chem.* **2021**, *56*, 283-9. DOI
38. Solati, N.; Karakaya, C.; Kaya, S. Advancing the understanding of the structure-activity-durability relation of 2D MoS_2 for the hydrogen evolution reaction. *ACS. Catal.* **2023**, *13*, 342-54. DOI
39. Singh, A. K.; Prasad, J.; Azad, U. P.; et al. Vanadium doped few-layer ultrathin MoS_2 nanosheets on reduced graphene oxide for high-performance hydrogen evolution reaction. *RSC. Adv.* **2019**, *9*, 22232-9. DOI
40. Shi, Y.; Zhou, Y.; Yang, D. R.; et al. Energy level engineering of MoS_2 by transition-metal doping for accelerating hydrogen evolution reaction. *J. Am. Chem. Soc.* **2017**, *139*, 15479-85. DOI
41. Hu, J.; Wu, J.; Zhang, S.; et al. One-pot Fabrication of 2D/2D $CdIn_2S_4/In_2S_3$ heterojunction for boosting photocatalytic Cr(VI) reduction. *Catalysts* **2023**, *13*, 826. DOI
42. Geng, X.; Singh, G.; Sathish, C.; et al. Biomass derived nanoarchitectonics of porous carbon with tunable oxygen functionalities and hierarchical structures and their superior performance in CO_2 adsorption and energy storage. *Carbon* **2023**, *214*, 118347. DOI
43. Ying, T.; Yu, T.; Qi, Y.; Chen, X.; Hosono, H. High entropy van der waals materials. *Adv. Sci.* **2022**, *9*, e2203219. DOI PubMed PMC
44. Kozdra, S.; Wójcik, A.; Das, T.; Michałowski, P. P. From DFT investigations of oxygen-implanted molybdenum disulfide to temperature-induced stabilization of MoS_2/MoO_3 heterostructure. *Appl. Sur. Sci.* **2023**, *631*, 157547. DOI
45. Zander, J.; Timm, J.; Weiss, M.; Marschall, R. Light-induced ammonia generation over defective carbon nitride modified with pyrite. *Adv. Energy. Mater.* **2022**, *12*, 2202403. DOI
46. Wolski, S. C.; Kuper, J.; Hänzelmann, P.; et al. Crystal structure of the FeS cluster-containing nucleotide excision repair helicase XPD. *PLoS. Biol.* **2008**, *6*, e149. DOI
47. Mahmood, N.; Yao, Y.; Zhang, J. W.; Pan, L.; Zhang, X.; Zou, J. J. Electrocatalysts for hydrogen evolution in alkaline electrolytes: mechanisms, challenges, and prospective solutions. *Adv. Sci.* **2018**, *5*, 1700464. DOI